nature COMMUNICATIONS

ARTICLE

DOI: 10.1038/s41467-017-00642-0 OPEN

Molecular analogue of the perovskite repeating unit and evidence for direct Mn^{III}-Ce^{IV}-Mn^{III} exchange coupling pathway

Annaliese E. Thuijs[1], Xiang-Guo Li[2], Yun-Peng Wang[2], Khalil A. Abboud[1], X.-G. Zhang[2], Hai-Ping Cheng[2] & George Christou[1]

The perovskite manganites $AMnO_3$ and their doped analogues $A_{1-x}B_xMnO_3$ (A and B = main group and lanthanide metals) are a fascinating family of magnetic oxides exhibiting a rich variety of properties. They are thus under intense investigation along multiple fronts, one of which is how their structural and physical properties are modified at the nanoscale. Here we show that the molecular compound $[Ce_3Mn_8O_8(O_2CPh)_{18}(HO_2CPh)_2]$ ($Ce^{III}_2Ce^{IV}Mn^{III}_8$; hereafter Ce_3Mn_8) bears a striking structural resemblance to the repeating unit seen in the perovskite manganites. Further, magnetic studies have established that Ce_3Mn_8 exhibits both the combination of pairwise Mn^{III}_2 ferromagnetic and antiferromagnetic exchange interactions, and the resultant spin vector alignments that are found within the 3-D *C*-type antiferromagnetic perovskites. First-principles theoretical calculations reveal not only the expected nearest-neighbor Mn^{III}_2 exchange couplings via superexchange pathways through bridging ligands but also an unusual, direct Mn^{III}–Ce^{IV}–Mn^{III} metal-to-metal channel involving the Ce^{IV} *f* orbitals.

[1] Department of Chemistry, University of Florida, Gainesville, FL 32611-7200, USA. [2] Department of Physics, University of Florida, Gainesville, FL 32611-7200, USA. Correspondence and requests for materials should be addressed to H.-P.C. (email: hping@ufl.edu)

Perovskite manganites continue to be a source of great interest in the scientific community owing to the fascinating and important physical properties they exhibit, such as colossal magnetoresistance and multiferroicity[1–6]. These materials have been proposed for important applications in many technological fields such as spintronics and information storage[7]. Detailed insights into the mechanisms by which these materials function has often been limited owing to their complex nature[8]. In many cases, the most direct way to understand complex systems can be to study a fragment of the larger structures, and one way to do this is to apply a molecular bottom-up approach to make 0-D species whose molecular properties can overcome many of the limitations and complexities encountered in the characterization and study of bulk 3-D materials and their nanoparticles[9].

Molecules possess certain important advantages over nanoparticles, including particle monodispersity, crystallinity, true solubility, and a stabilizing shell of organic ligands that is also often capable of facile modification as desired. Given the success of molecular approaches to monodisperse nanoscale magnets in other areas such as single-molecule magnetism, the synthesis and study of molecules with a structural resemblance to the perovskites would provide an alternative and complementary approach to ultra-small perovskite nanoparticles. Such advantages of molecules over their bulk counterparts for study of known physical phenomena, and discovery of new ones, are well documented in the field of single-molecule magnets (SMMs)[10, 11]. These are 0-D molecular nanomagnets that possess a combination of uniaxial anisotropy and a high ground state spin, and consequently function as superparamagnets below their blocking temperatures, T_B[12–16]. In a similar fashion, attainment of molecular species that combine the structural and physical properties of the perovskite manganites would provide an ideal and alternative route forward for understanding the origins of the properties of this important class of materials, including ultimately those with multiferroic behavior.

In the present work, we prepare and study a molecular compound $[Ce_3Mn_8O_8(O_2CPh)_{18}(HO_2CPh)_2]$ ($Ce^{III}_2Ce^{IV}Mn^{III}_8$; hereafter Ce_3Mn_8) that is structurally reminiscent of the repeating unit in perovskite manganites. Magnetic characterization shows that the spin vector alignments in this molecule are the same as in the 3-D *C*-type antiferromagnetic perovskites. First-principles theoretical calculations reveal an unusual and direct Mn^{III}–Ce^{IV}–Mn^{III} metal-to-metal magnetic exchange channel involving the Ce^{IV} *f* orbitals, besides the conventional nearest-neighbor Mn^{III}_2 exchange couplings via superexchange pathways through bridging ligands. An excellent agreement between theory and experiment for the magnetic susceptibility curve is reached along with the establishment of an unprecedentedly rich physical picture of magnetic interaction. The work demonstrates the feasibility of a bottom-up molecular approach to gaining insights into the structural and physical properties of ultra-small nanoscale perovskite materials, as well as surface units on larger particles where structural relaxation effects and O vacancies are present.

Results

Synthesis and structure characteristics. 3-D perovskites are prepared at high temperatures in the solid state, whereas 0-D molecules are typically prepared at or near ambient temperatures in solution. The results reported here were thus crucially dependent on the successful development of an experimental procedure for the synthesis of pure, crystalline Ce_3Mn_8 (see "Methods"). The structure (Fig. 1) was determined by single-crystal X-ray diffractometry (Supplementary Methods and Supplementary Tables 1–3) and consists of a $\{Ce^{IV}Mn^{III}_8(\mu_3\text{-}O)_8\}^{12+}$ unit comprising a Mn_8 distorted cube with a Ce^{IV} at its center held together by four μ_3-O^{2-} and four μ_4-O^{2-} ions, with the latter connecting to two external Ce^{III} ions attached on opposite faces of the cube. The organic ligation consists of two μ_4-, four μ_3-, and twelve μ_2-benzoate

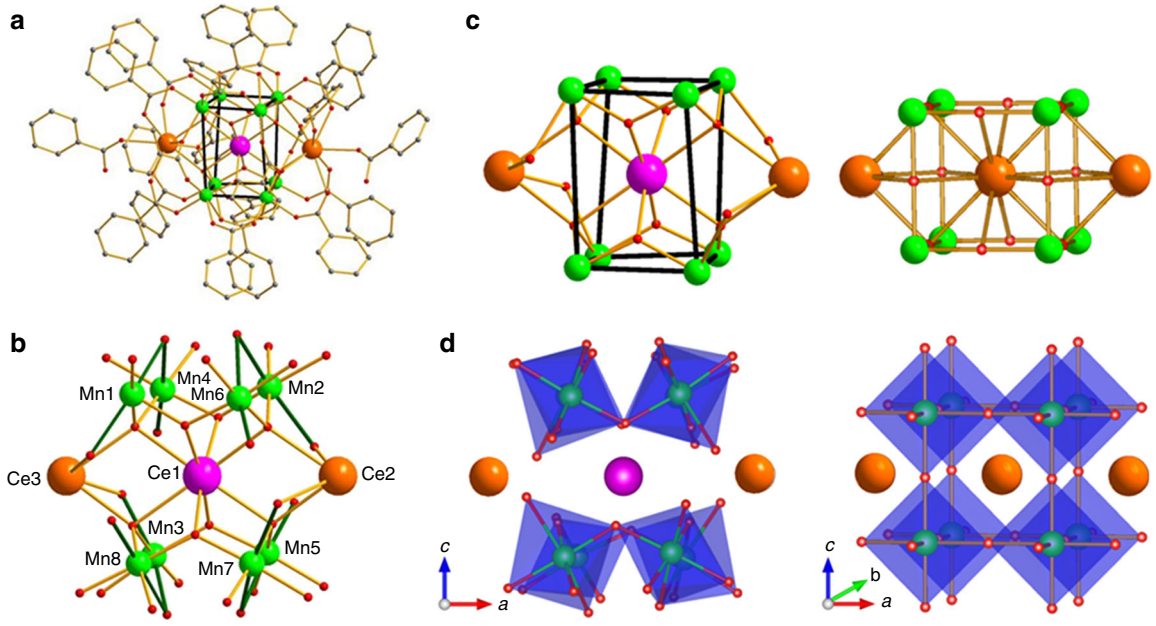

Fig. 1 The molecular structure of Ce_3Mn_8 from experimental single-crystal X-ray diffractometry data. **a** The complete structure with H atoms omitted for clarity. The *thicker black lines* are guides to the eye to emphasize the distorted Mn_8 cube. **b** The partially labeled central fragment with the Mn^{III} JT axes indicated as thicker Mn–O bonds. Color scheme: Ce^{IV} *purple*; Ce^{III} and Ln^{III} *orange*; Mn^{III} *green*; O *red*; C *gray*. **c** Comparison of the core from (**a**) of Ce_3Mn_8 (*left*) with a repeating unit of an ideal ABO_3 cubic perovskite plus two A ions from adjacent repeating units (*right*). **d** As for (**c**) but showing the MnO_6 polyhedra

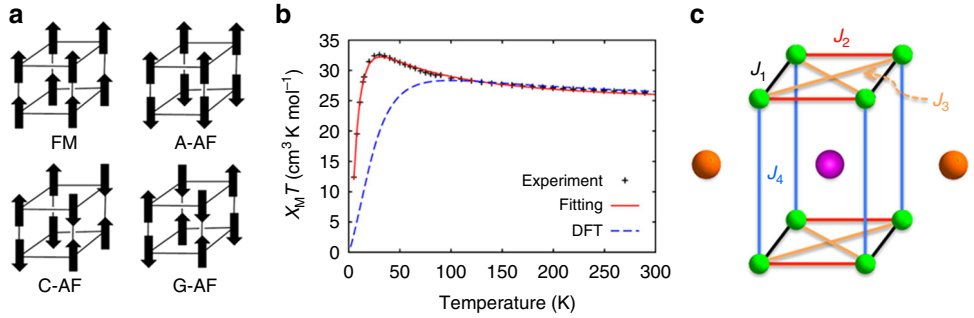

Fig. 2 Magnetic properties of Ce_3Mn_8 and perovskites. **a** Four known spin-ordering configurations in a perovskite unit cell. **b** Experimental $\chi_M T$ vs T plot for Ce_3Mn_8 in a 1 kG applied dc field (+), with the small contributions from the two external Ce^{III} ions subtracted. *Solid* and *dashed lines* are theoretical results from a multi-spin Heisenberg model using either exchange coupling J's and anisotropy term D from fits to the experimental data (*solid line*) or calculated from first-principles DFT (*dashed line*). **c** The multi-spin Heisenberg model showing the magnetic exchange coupling paths labeled as J_1 to J_4; *colored lines* indicate symmetry-equivalent sets. Other possible paths (unlabeled) correspond to exchange coupling strengths at least an order of magnitude smaller than the ones labeled in the figure

groups, as well as two terminal benzoic acid groups on the Ce^{III} ions. All Mn^{III} atoms are six-coordinate with distorted octahedral geometries and exhibit Jahn–Teller (JT) distortion (elongation) axes. The latter are localized, meeting in pairs at the O atoms of the μ_4-benzoate groups (Fig. 1b). The Ce^{III} and Ce^{IV} ions are nine-coordinate and eight-coordinate, respectively.

The core of Ce_3Mn_8 is overall similar to a fragment of the cubic perovskite structure, shown in Fig. 1c for comparison, where it can be seen to comprise a $LnMn^{III}{}_8O_x$ (Ln = lanthanide) unit plus two additional Ln ions that in a 3-D perovskite array would be in the adjacent repeating units. It can thus be described as one complete and two partial repeating units of the perovskite structure. Also notable is that it exhibits distinct distortions from cubic symmetry and that some of these are similar to those seen in the $LnMn^{III}O_3$ manganites. This is particularly interesting as Ce_3Mn_8 is a discrete molecular complex buffered by the organic ligation from external influences, whereas many distortions within the more rigid 3-D perovskite structure are cooperative in nature. In Ce_3Mn_8: firstly, the cube undergoes a tetragonal distortion (stretching) along one direction due to the JT axis locations and the external Ce ions, giving short and long Mn… Mn edge separations of 3.16–3.33 Å and 4.84–4.94 Å, respectively; secondly, the MnO_6 octahedra are tilted, allowing the bridging O^{2-} ions to move off the Mn–Mn edges and toward the center of the cube to optimize Ce–O bond lengths; and thirdly, the long Mn... Mn edges are bridged by longer $PhCO_2^-$groups rather than shorter O^{2-} bridges, so that the corresponding core is $\{CeMn_8O_8(O_2CPh)_4\}$ vs $\{CeMn_8O_{12}\}$ for the perovskite. The first point is reminiscent of, although of greater magnitude than the tetragonal perovskite structures, and the second point is reminiscent of the orthorhombic structure of the perovskite $LnMnO_3$ manganites, where a distortion involving tilting of the MnO_6 octahedra (by an amount dependent on the Ln ionic radius) away from the ideal cubic structure similarly arises from the combined effect of Mn^{III} JT distortions and a mismatch of the Ln–O and Mn–O bond lengths, moving the oxide ions off the Mn–Mn edges[17]. Interestingly, the above three points together suggest that Ce_3Mn_8 may best be considered a model for surface-repeating units of perovskite nanoparticles, where structural relaxation effects and oxide ion vacancies are present. Further comparison between Ce_3Mn_8 and the corresponding Ln = Ce manganite $CeMnO_3$ is precluded by the absence of crystallographic information for this material[18], which appears to be difficult to synthesize pure due to the multiple oxidation states accessible to both cerium and manganese.

Magnetic structure analysis. The location and orientation of the Mn^{III} Jahn–Teller axes in Ce_3Mn_8 (Fig. 1b and Supplementary Table 3) represent the local Mn z axes and thus the location of the singly occupied σ-symmetry $d_z{}^2$ orbitals. When two $d_z{}^2$ (d_σ) orbitals meet at a bridging O atom with the acute Mn–O–Mn angles (83–88°) in Ce_3Mn_8, the empirical Goodenough–Kanamori (GK) rules[19–21] predict ferromagnetic (FM) interactions for the Mn1/Mn4, Mn2/Mn6, Mn3/Mn8, and Mn5/Mn7 pairs (Fig. 1b). Exchange couplings for the other Mn^{III} pairs are expected to be dominated by overlap of d_π magnetic orbitals, and thus to be weakly antiferromagnetic (AF) according to the GK rules. For perovskite manganites, competition among spin, charge, and orbital degrees of freedom determine the magnetic properties, and the Mn^{III} JT axes are intimately involved[22]. Depending on the precise orbital ordering and the associated superexchange interactions in a given manganite, a particular combination of FM and AF interactions emerges[23]. The common types of spin ordering that result (ferromagnetic or FM, and three types of AF: A-AF, C-AF, and G-AF) for this structure are illustrated in the *left panel* of Fig. 2. Below we describe the experimental magnetic data for Ce_3Mn_8 and then we will apply first-principles electronic structure calculations to reveal the microscopic mechanics of magnetic coupling in the Ce_3Mn_8 molecule, thereby providing a unique angle for understanding the exchange interactions in perovskite manganites.

Experimental solid-state magnetic susceptibility (χ_M) data on Ce_3Mn_8 were collected on a microcrystalline sample, restrained in eicosane to prevent torquing, in a 1 kG (0.1 T) field in the 5–300 K range. The obtained $\chi_M T$ vs T plot (*middle panel* in Fig. 2) exhibits two regimes, increasing from 26.80 $cm^3\,Kmol^{-1}$ at 300 K to a maximum of 32.68 $cm^3\,Kmol^{-1}$ at 30 K, and then steeply decreasing to 12.41 $cm^3\,Kmol^{-1}$ at 5 K. The value at 300 K is greater than the 25.62 $cm^3\,Kmol^{-1}$ calculated for eight Mn^{III} ($S = 2$, $\chi_M T = 3$ $cm^3\,Kmol^{-1}$ with $g = 2$) and two Ce^{III} (f^1, $S = ½$, $L = 3$, $^2F_{5/2}$, $\chi_M T = 0.81$ $cm^3\,Kmol^{-1}$)[24] non-interacting ions, indicating the increasing $\chi_M T$ with decreasing T to be due to dominant FM pairwise $Mn^{III}Mn^{III}$ interactions within the molecule. The steep decrease below 30 K is assigned to weaker AF interactions that begin to pair-up spins at lower temperatures. $\chi_M T$ is clearly heading for a small value at ~0 K, indicating a ground state spin description for Ce_3Mn_8 as an AF $S = 0$ Mn_8 cube, and two essentially non-interacting Ce^{III} ions as expected from the very weak exchange couplings exhibited by Ln^{III} ions[25]. This description is supported by the in-phase ac susceptibility

Table 1 Total energy (*E*) and atomically resolved magnetic moments (*M*[a]) due to valence electrons for different sites of Ce_3Mn_8 in different spin-ordered states

Spin order	$E^{b,c}$	abs($M_{Ce^{IV}}$)[d]	$M_{Ce^{IV}}$	abs(M_{Mn})	M_{Mn}	abs(M_O)	M_O	$M_{C,H}$	M_{total}
FM	19	0.28	0.28	28.57	28.57	2.97	2.97	0.17	32.00
A-AF-I	37	0.00	0.00	28.30	−0.06	2.06	0.06	0.00	0.00
A-AF-II	14	0.03	0.03	28.55	0.03	2.81	0.01	0.01	0.00
A-AF-III	10	0.03	0.00	28.22	0.04	2.17	−0.03	−0.01	0.00
C-AF-I	0	0.02	−0.02	28.20	0.04	1.99	−0.02	0.00	0.00
C-AF-II	99	0.00	0.00	27.99	−0.04	1.50	0.04	0.00	0.00
C-AF-III	19	0.02	−0.01	28.28	−0.06	1.85	0.07	0.00	0.00
G-AF	85	0.01	0.01	27.99	0.02	1.31	−0.04	0.01	0.00

[a] $M = N^{\uparrow} - N^{\downarrow}$, $N^{\uparrow(\downarrow)}$ is the spin-up (down) charge density
[b] In meV
[c] The energy of state C-AF-I (the ground state) is set to 0
[d] abs(*M*) is the total absolute magnetization, in μ_B

($\chi'_M T$) vs T plot down to 1.8 K (Supplementary Fig. 1), which extrapolates to a small non-zero value consistent with the expected $\chi_M T = 1.62\ cm^3\ Kmol^{-1}$ for two independent Ce^{III} ions.

First-principles energetics. To characterize the origin of the AF ground state of Ce_3Mn_8, the magnetic properties of Ce_3Mn_8 were calculated within the framework of Kohn–Sham density functional theory (DFT), using atomic coordinates for the molecule taken from the crystal structure. DFT based methods have been widely used for studying molecular magnets with Mn centers[26–31]. First-principles calculations were performed for eight different spin configurations of Ce_3Mn_8 molecules, corresponding to FM, A-AF, C-AF, and G-AF spin alignments (Supplementary Methods), with all three orientations of the ferromagnetic planes (A-AF) or axes (C-AF) considered and neglecting any noncolinearity (the easy axis is assumed to be along the global z axis). The results (Table 1) show that spin state C-AF-I has the lowest total energy. The absolute magnetization of each Mn ion is ~3.5 μ_B, as expected for Mn^{III} with some induced magnetization at the O sites. Each of the two outer Ce^{III} sites has a magnetic moment of 1 μ_B, which is included in the core region of the charge density. In the FM state, the central Ce^{IV} site has a small magnetic moment (0.28 μ_B) and, as expected, no net spin density is found on the Ce^{IV} sites for any of the $S = 0$ AF states. The C-AF-I ground state corresponds to FM coupling in the b direction (i.e., the Mn1/Mn4, Mn2/Mn6, Mn3/Mn8, and Mn5/Mn7 pairs of Fig. 1b) and net AF coupling along the a and c directions, as suggested by the qualitative predictions from the structural parameters and $\chi_M T$ vs T data. The weak net AF coupling is supported by the low-lying A-AF-II and A-AF-III excited states, corresponding to different relative alignments of the four FM pairs. The energy difference ΔE between the ground state and the FM state is about 19 meV, corresponding to a switching magnetic field of $B = \Delta E/g\mu_B\Delta M \approx 5$ T (to switch from C-AF-I to FM), where ΔM is the magnetic moment difference, $\mu_B = 0.058\ meV/T$, and $g = 2$. A plot of $M/N\mu_B$ vs applied magnetic field (Supplementary Fig. 2) steadily increases and appears to be heading for saturation in the expected $M/N\mu_B$ range of $gS = 32$ for $S = 16$, or in fact a little less as $g < 2$ slightly for Mn^{III}.

Theoretical analysis of the magnetic properties. The DFT results were further analyzed using a multi-spin model, defined by the spin Hamiltonian of Eq. (1) in Supplementary Methods, to estimate the various pairwise Mn/Mn exchange coupling parameters (J). Four spin coupling paths (denoted by J_1 through J_4 in the *right panel* of Fig. 2) were found to have significant contributions to the total energy. J_1 appears to involve a conventional superexchange mechanism via two monoatomically bridging oxygens. This was predicted above to be strongly FM by the GK rules. J_2 appears to involve two parallel superexchange pathways: one via a single monoatomically bridging oxygen and the other through a carboxylate group (Mn–O–CR–O–Mn, R = phenyl). Both J_3 and J_4 appear at first glance to involve mostly superexchange through carboxylate groups; the Mn–Mn distances are 4.6 Å and 4.9 Å for the J_3 and J_4 pathways, respectively (compared to 3.16–3.33 Å for J_1 and J_2). Initial calculations using the symmetry broken DFT method and incorporating J_1–J_4 showed that J_4 was, consistent with the structure, much weaker than J_1–J_3 and AF. In fitting experimental data, we therefore omit J_4 but include the axial anisotropy parameter (D) as even with current supercomputers it is not feasible to include both D and four J's due to the excessive memory requirement. Our calculations show that the anisotropy easy axis is along the global z direction, perpendicular to the Mn1–Mn4–Mn2–Mn6 and Mn3–Mn5–Mn7–Mn8 planes. The calculated coupling strengths (positive for FM, negative for AF) and D were $J_1 = +1.61$ meV ($+13\ cm^{-1}$), $J_2 = +0.72$ (+5.8), $J_3 = -1.10$ (−8.87), and $D = -0.07$ (−0.56).

The $\chi_M T$ vs T plot generated using the calculated DFT parameters is only in fair agreement with the experimental data (Fig. 2, *dashed line* in *middle panel*), missing the continuing rise in $\chi_M T$ below 100 K and the peak at 30 K, before the steep decrease at lower temperatures. Therefore, the J_1–J_3 and D values were refined by fitting the experimental $\chi_M T$ vs T data directly to the multi-spin Heisenberg model using the calculated DFT parameters as input values. An excellent fit was now obtained (Fig. 2, *solid line*) with $J_1 = +1.26$ meV ($+10.2\ cm^{-1}$), $J_2 = +0.69$ (+5.6), $J_3 = -0.74$ (−6.0), and $D = -0.05$ (−0.40), again resulting in a C-AF-I ground state.

Discussion

The above results present a consistent picture of a dominating J_1 FM interaction and a C-AF ground state spin configuration. In fact, as J_2 is also FM, the C-AF ground state is driven by the AF J_3 coupling, the diagonal Mn_2 interaction. It is comparable in magnitude to J_2 and there is competition (spin frustration) between the J_1, J_2, and J_3 couplings in the Mn_3 triangles within each Mn_4 square at the top and bottom of the molecule (Fig. 2). J_1 dominates giving four FM Mn_2 pairs, but the relative alignment of these pairs to give the C-AF-I ground state is caused by the slightly stronger J_3 vs J_2, i.e., $|J_3| > |J_2|$, and the AF J_4. If $|J_3| < |J_2|$, however, then the ground state would have been A-AF, the A-AF-II state in Supplementary Methods. The Ce_3Mn_8 ground state is thus dependent on the relative values of J_2 vs J_3: the former is clearly mediated by the superexchange pathways through

the O^{2-} and RCO_2^- bridges but is opposite of the expected weakly AF character according to GK rules. Thus, we sought further insight into this unexpected result as well as the origin of the diagonal J_3.

The DFT calculations allow us to analyze the microscopic electronic and magnetic processes responsible for the magnetic couplings. The sign of J_2 suggests that the unoccupied Ce^{IV}-4*f* orbitals residing at the upper edge of the energy gap may have an unexpectedly important role in magnetic couplings. To reveal its role, we carried out an additional DFT calculation by replacing the Ce ions in Ce_3Mn_8 with La ions, and made the La_3Mn_8 molecule negatively charged to preserve the Mn^{III} valence state. In contrast to Ce_3Mn_8, the La-4*f* orbitals in $[La_3Mn_8]^-$ are ~2.5–3.5 eV above the energy gap (Supplementary Discussion), and thus are not expected to contribute to magnetic couplings. J_1 to J_4 in the $[La_3Mn_8]^-$ molecule are more AF by ~0.1–0.8 meV (0.8–6.5 cm^{-1}) than those in Ce_3Mn_8 (Supplementary Discussion). The comparison between Ce_3Mn_8 and La_3Mn_8 indicates that the contribution of Ce^{IV}-4*f* orbitals in Ce_3Mn_8 is FM in nature, as we further explain below. The magnetic coupling among Mn^{III} ions in these molecules can be decomposed into two contributions from different physical origins: the AF superexchange coupling via bridging O^{2-} ions and/or carboxylate groups, and a FM direct exchange coupling enhanced by the Ce^{IV} ion. The strength of the superexchange coupling is determined by the effective hopping integral between Mn-d_z^2 states of two Mn ions. The integral can be calculated by downfolding the DFT Hamiltonian onto Mn-d_z^2 orbitals using the maximally localized Wannier function method[32]. The calculated effective hopping integrals in Ce_3Mn_8 molecule are almost the same as those in $[La_3Mn_8]^-$ (Supplementary Discussion). From this, we conclude that the same AF superexchange couplings exist in both molecules, and rule out a possible AF superexchange coupling via Ce^{IV}-4*f* orbitals. The FM direct exchange depends on the shape of Mn-3*d* orbitals. The presence of Ce^{IV}-4*f* orbitals near the energy gap enhances the direct exchange coupling between neighboring Mn pairs by pulling the Mn-d_z^2 orbitals closer to each other through hybridization with the Ce^{IV}-4*f* orbitals and forming an itinerant electron path between two Mn ions. Indeed, the shape of Mn-d_z^2 Wannier orbitals shows considerable difference between Ce_3Mn_8 and $[La_3Mn_8]^-$ (Supplementary Discussion). The overall picture that emerges is an unexpected FM contribution to the Mn_2 exchange couplings from a direct Mn–Ce–Mn pathway, making J_2 FM and comparable in absolute magnitude to J_3, leading to a C-AF ground state but with low-lying A-AF excited states. This suggests that small structural distortions (e.g., from applied pressure, changes in the identity of the ligands, etc.) could alter the J_2:J_3 ratio and switch the ground state to A-AF.

Overall, a synthetic method has been developed to a Ce_3Mn_8 cluster that shows strong structural similarity to the repeating unit of perovskite manganites. It exhibits two structural distortions common in bulk ABO_3 perovskites, namely tilting of the BO_6 octahedra and a tetragonal distortion driven by JT elongation of the B cations, and it also exhibits the same spin ordering as *C*-type antiferromagnetic perovskites. This demonstrates that these unusual structural and spin-ordering effects can be reproduced even at the level of a single repeating unit. We propose Ce_3Mn_8 may also be particularly relevant to surface units of nanoscale perovskites. First-principles-based investigations reveal the microscopic mechanism of the magnetic couplings inside the Ce_3Mn_8 molecule. The unoccupied Ce^{IV}-4*f* orbitals have considerable contribution to the direct exchange coupling, which in turn has a pivotal role in the competition (spin frustration) between FM and AF interactions in this molecule and the resulting ground state C-AF spin configuration with low-lying A-AF excited states. These results suggest analogous effects may be important in the magnetic couplings within the extended lattices of Ce^{IV}-containing perovskites or similar compounds in which 4*f* orbitals can be brought close to the Fermi energy. Attempts to complete one or both partial cubes at each end of Ce_3Mn_8 with additional Mn^{III} ions to yield a molecule representing two or three face-fused repeating perovskite units are in progress, as is the synthesis of Ce_3Mn_8 analogues with various other lanthanide or main group metal ions to expand the experimental database. New molecules of this type, analogues to the $BiMnO_3$ or $TbMnO_3$ systems, may even show true multiferroic bistability and further shed light on the complex mechanisms involved in these systems.

Methods

Experiments. The comproportionation reaction of $Mn(O_2CPh)_2{\cdot}2H_2O$, $Ce(NO_3)_3{\cdot}6H_2O$, $NBu^n_4MnO_4$ and $PhCO_2H$ in a 4:4:1:16 molar ratio in $MeNO_2$ at ~80 °C gave a dark brown solution from which was isolated $[Ce_3Mn_8O_8(O_2CPh)_{18}(HO_2CPh)_2]$ (Ce_3Mn_8) as black crystals in ~55% yield based on Mn (Supplementary Methods). Single-crystal X-ray diffraction studies at 100 K were performed on a Bruker DUO diffractometer using MoK_α ($\lambda = 0.71073$ Å) or CuK_α ($\lambda = 1.54178$ Å) radiation (from an ImuS power source), and an APEXII CCD area detector. The metal oxidation states and the oxygen protonation levels were confirmed by charge considerations and bond valence sum calculations (Supplementary Tables 1, 2)[33, 34].

Computations. Electronic and magnetic properties of the Ce_3Mn_8 molecule were calculated within the framework of Kohn–Sham DFT[35] using the spin-polarized Perder–Burke–Ernzehof[36] exchange correlation functional and project-augmented wave[37, 38] pseudopotentials in conjuction with the plan-wave basis as implemented in the Vienna Ab-initio Simulation Package[39, 40]. The plane-wave cutoff energy was 500 eV, and the energy threshold for self-consistency was 10^{-5} eV. Owing to the strong localization of the Ce *f* electron, the GGA + *U* method was applied with $U = 2$ eV[41] for the Ce *f* orbitals. Spin–orbit interactions were also included.

Data availability. The crystallographic information file (CIF) for $[CeMn_8O_8(O_2CPh)_{18}(HO_2CPh)_2]{\cdot}x$(solvent) ($Ce_3Mn_8$) has been deposited at the Cambridge Crystallographic Data Centre with deposition code CCDC 1533475.

Received: 23 December 2016 Accepted: 17 July 2017
Published online: 11 September 2017

References

1. Cheong, S.-W. & Mostovoy, M. Multiferroics: a magnetic twist for ferroelectricity. *Nat. Mater.* **6**, 13–20 (2007).
2. Maignan, A., Martin, C., Hebert, S. & Hardy, V. Colossal magnetoresistance manganites: importance of the coorperative phenomena. *J. Mater. Chem.* **17**, 5023–5031 (2007).
3. Harris, A. B., Kenzelmann, M., Aharony, A. & Entin-Wohlman, O. Effect of inversion symmetry on the incommensurate order in multiferroic RMn_2O_5 (R=rate earth). *Phys. Rev. B* **78**, 014407 (2008).
4. Dong, S. & Liu, J.-M. Recent progress of multiferroic perovskite manganites. *Mod. Phys. Lett. B* **26**, 1230004 (2012).
5. Salamon, M. & Jaime, M. The physics of manganites: structure and transport. *Rev. Mod. Phys.* **73**, 583–628 (2001).
6. Schmid, H. Multi-ferroic magnetoelectics. *Ferroelectrics* **162**, 317–338 (1994).
7. Picozzi, S. & Ederer, C. First principles studies of multiferroic materials. *J. Phys. Condens. Matter.* **21**, 303201 (2009).
8. Eerenstein, W., Mathur, N. D. & Scott, J. F. Multiferroic and magnetoelectric materials. *Nature* **442**, 759–765 (2006).
9. Hendrickson, D. N. et al. Half-integer spin molecular nanomagnets. *MRS Proc.* **746**, Q1.1 (2002).
10. Bogani, L. & Wernsdorfer, W. Molecular spintronics using single-molecule magnets. *Nat. Mater.* **7**, 179–186 (2008).
11. Friedman, J. R. & Sarachik, M. P. Single-molecule nanomagnets. *Ann. Rev. Condens. Matter Phys.* **1**, 109–128 (2010).
12. Sessoli, R. et al. High-spin molecules: $[Mn_{12}O_{12}(O_2CR)_{16}(H_2O)_4]$. *J. Am. Chem. Soc.* **115**, 1804–1816 (1993).
13. Christou, G., Gatteschi, D., Hendrickson, D. N. & Sessoli, R. Single-molecule magnets. *MRS Bull.* **25**, 66–71 (2000).
14. Christou, G. Single-molecule magnets: a molecular approach to nanoscale magnetic materials. *Polyhedron* **24**, 2065–2075 (2005).

15. Sessoli, R., Gatteschi, D., Caneschi, A. & Novak, M. A. Magnetic bistability in a metal-ion cluster. *Nature* **365**, 141–143 (1993).
16. Wernsdorfer, W., Aliaga-Alcalde, N., Hendrickson, D. N. & Christou, G. Exchange-biased quantum tunneling in a supramolecular dimer of single-molecule magnets. *Nature* **416**, 406–409 (2002).
17. Tachibana, M., Shimoyama, T., Kawaji, H., Atake, T. & Takayama-Muromachi, E. Jahn–Teller distortion and magnetic transitions in perovskite $RMnO_3$ (R = Ho, Er, Tm, Yb, and Lu). *Phys. Rev. B* **75**, 144425 (2007).
18. Ambrunaz-Quezel, S. Neutron-diffraction-determined parameters of manganates of the rare earths of perovskite type and magnetic structures in praseodymium manganate(III) ($PrMnO_3$) and neodymium manganate(III) ($NdMnO_3$). *Bull. Soc. Fr. Mineral. Cristallogr.* **91**, 339 (1968).
19. Goodenough, J. B. Theory of the role of covalence in the perovskite-type manganites [La,M]MnO_3. *Phys. Rev.* **100**, 564–573 (1955).
20. Goodenough, J. B. An interpretation of the magnetic properties of the perovksite-type mixed crystals $La_{1-x}Sr_xCoO_3$. *J. Phys. Chem. Solids* **6**, 287–297 (1958).
21. Kanamori, J. Superexchange interaction and symmetry properties of electron orbitals. *J. Phys. Chem. Solids* **10**, 87–98 (1959).
22. Koppel, H., Yarkony, D. R. & Barentzen, H. *The Jahn–Teller Effect* (Springer, 2009).
23. Hotta, T., Yunoki, S., Mayr, M. & Gagotto, E. A-type antiferromagnetic and C-type orbital-ordered states in $LaMnO_3$ using cooperative Jahn–Teller phonons. *Phys. Rev. B* **60**, R15009–R15012 (1999).
24. Kahn, O. *Molecular Magnetism* (Wiley-VCH, 1993).
25. Sessoli, R. & Powell, A. K. Strategies towards single molecule magnets based on lanthanide ions. *Coord. Chem. Rev.* **253**, 2328–2341 (2009).
26. Pederson, M. R. & Khanna, S. N. Magnetic anisotropy barrier for spin tunneling in $Mn_{12}O_{12}$ molecules. *Phys. Rev. B* **60**, 9566–9572 (1999).
27. Park, K., Pederson, M. R., Richardson, S. L., Aliaga-Alcalde, N. & Christou, G. Density-functional theory calculation of the intermolecular exchange interaction in the magnetic Mn_4 dimer. *Phys. Rev. B* **68**, 020405 (2003).
28. Postnikov, A. V., Kortus, J. & Pederson, M. R. Density functional studies of molecular magnets. *Phys. Stat. Sol.* **243**, 2533–2572 (2006).
29. Ruiz, E. et al. Magnetic structure of the large-spin Mn_{10} and Mn_{19} complexes: a theoretical complement to an experimental milestone. *J. Am. Chem. Soc.* **130**, 7420–7426 (2008).
30. Wu, Y.-N., Zhang, X.-G. & Cheng, H.-P. Giant molecular magnetocapacitance. *Phys. Rev. Lett.* **110**, 217205 (2013).
31. Li, X.-G., Fry, J. N. & Cheng, H.-P. Single-molecule magnet Mn_{12} on graphene. *Phys. Rev. B* **90**, 125447 (2014).
32. Marzari, M., Mostofi, A. A., Yates, J. R., Souza, I. & Vanderbilt, D. Maximally localized Wannier functions: theory and applications. *Rev. Mod. Phys.* **84**, 1419–1475 (2012).
33. Liu, W. & Thorp, H. H. Bond valence sum analysis of metal-ligand bond lengths in metalloenzymes and model complexes. 2. Refined distance and other enzymes. *Inorg. Chem.* **32**, 4102–4105 (1993).
34. Roulhac, P. L. & Palenik, G. J. Bond valence sums in coordination chemistry. The calculation of the oxidation state of cerium in complexes containing cerium bonded only to oxygen. *Inorg. Chem.* **42**, 118–121 (2003).
35. Kohn, W. & Sham, L. J. Self-consistent equations including exchange and correlation effects. *Phys. Rev.* **140**, A1133–A1138 (1965).
36. Perdew, J. P., Burke, K. & Ernzerhof, M. Generalized gradient approximation made simple. *Phys. Rev. Lett.* **77**, 3865–3868 (1996).
37. Blochl, P. E. Projector augmented-wave method. *Phys. Rev. B* **50**, 17953–17979 (1994).
38. Kresse, G. & Joubert, J. From ultrasoft pseudopotentials to the projector augmented wave method. *Phys. Rev. B* **59**, 1758–1775 (1999).
39. Kresse, G. & Furthmuller, J. Efficiency of an-initio total energy calculations for metals and semiconductors using a plane-wave basis set. *Comput. Mater. Sci.* **6**, 15–50 (1996).
40. Kresse, G. & Furthmuller, J. Efficient iterative schemes for ab initio total-energy calculations using a plane-wave basis set. *Phys. Rev. B* **54**, 11169–11186 (1996).
41. Loschen, C., Carrasco, J., Neyman, K. M. & Illas, F. First-principles LDA + U and GGA + U study of cerium oxides: dependence on the effective U parameter. *Phys. Rev. B* **75**, 035115 (2007).

Acknowledgements

This work was supported by the US National Science Foundation DMREF program under Grant No. CHE-1534401, and partially supported by Grant CHE-1565664. Calculations were performed at the National Energy Research Scientific Computing Center and at UF Research Computing.

Author contributions

This project was designed and directed by H.-P.C., G.C., and X.-G.Z. A.E.T. and K.A.A. performed the experiments and analyzed the experimental data. X.-G.L. and Y.-P.W. performed the first-principles and numerical calculations, and analyzed the experimental data. All authors contributed to writing the manuscript.

Additional information

Supplementary Information accompanies this paper at doi:10.1038/s41467-017-00642-0.

Competing interests: The authors declare no competing financial interests.

Reprints and permission information is available online at http://npg.nature.com/reprintsandpermissions/

Publisher's note: Springer Nature remains neutral with regard to jurisdictional claims in published maps and institutional affiliations.